Concept Design of a 5 MW Axial Flux Partially Superconducting Electric Machine

Thomas Tallerico[1], Aaron D. Anderson[2], and Justin Scheidler[3]
NASA Glenn Research Center, Cleveland, OH, 44135, United States

Single aisle class and larger electric and hybrid electric airplanes require high performance electric machines with power levels greater than 1 MW. Partially superconducting machines with superconducting rotors cooled by cryocoolers and non-cryogenic stators are possible solutions for meeting the machine performance requirements. In this paper, a conceptual design for a double-stator single-rotor axial-flux partially superconducting machine is presented. A design tool for the topology is presented and used to generate an initial concept design. High fidelity analysis of the concept design is used to assess the feasibility of the concept design to meet its target performance metrics and to identify areas of refinement for the next iteration of the design tool and resulting design.

I. Introduction

Single aisle class electrified aircraft have the potential to reduce aviation industry emissions and energy consumption per passenger mile. To enable these benefits, these vehicles require high specific power and efficiency electric drivetrains [1]. NASA's SUbsonic Single Aft eNgine (SUSAN) electrofan (Figure 1) is a regional jet concept vehicle targeting 50% emissions reduction relative to typical regional jets of 2024 through the implementation of various technologies [2]. One of the primary technologies implemented to enable the emissions reduction is a distributed hybrid electric propulsion system. The preliminary details of this propulsion system are provided in [3] and [4]. The propulsion system requires four 5 MW generators to extract power from the aircraft's single aft engine and deliver it to 16 wing propulsors. For SUSAN to meet its emissions goals, the target machine performance goal for the generators is 99% efficiency at 25 kW/kg.

In [5], the authors presented a first concept design for the SUSAN generators. Air-core and iron-core variants of radial-flux, partially-superconducting machines were considered, and a single air-core concept design was detailed. That design was predicted to achieve 22 kW/kg and 99.04% efficiency after high-fidelity analysis. In this paper, the design space is expanded to include axial-flux, air-core, partially-superconducting machines. Design trade space exploration is carried out with NASA's previously developed design methodologies for partially-superconducting machines [5] [6] [7]. A selected axial-flux design from the design studies is detailed and analyzed at a preliminary design level to assess the accuracy of the design tool's predicted performance of an axial-flux, partially-superconducting machine. The resulting machine design has an estimated specific power of 19 kW/kg and efficiency of 99% after high-fidelity analysis. This performance is below the target, but areas for further design refinement are noted that may enable this machine topology to meet the SUSAN specifications.

The machine designs in this paper build on the design of NASA's 1.4 MW High Efficiency Megawatt Motor (HEMM) [8] [9] [10] [11] [12] [13] [14]. A wound-field, partially-superconducting topology with a cryogenic, superconducting rotor and non-cryogenic, liquid-cooled stator is assumed for all designs. The superconducting rotor is assumed to be cooled by an in-shaft cryocooler such that the machine requires no additional cryogenic systems on the aircraft. Herein, the cryocooler is a second generation of the HEMM cryocooler, which is being developed in parallel and is not detailed in this paper.

Section II of this paper details the machine's requirements. Section III describes the design tool for the axial-flux machines. Section IV presents design trade space exploration results. Section V presents a design refinement based

[1] Aerospace Research Engineer, Rotating and Drive Systems
[2] Electrical Engineer, Diagnostics and Electromagnetics
[3] Aerospace Research Engineer, Rotating and Drive Systems

on 2D finite element analysis (FEA). Section VI presents the detailed design of an example axial-flux generator. Section VII provides a conclusion.

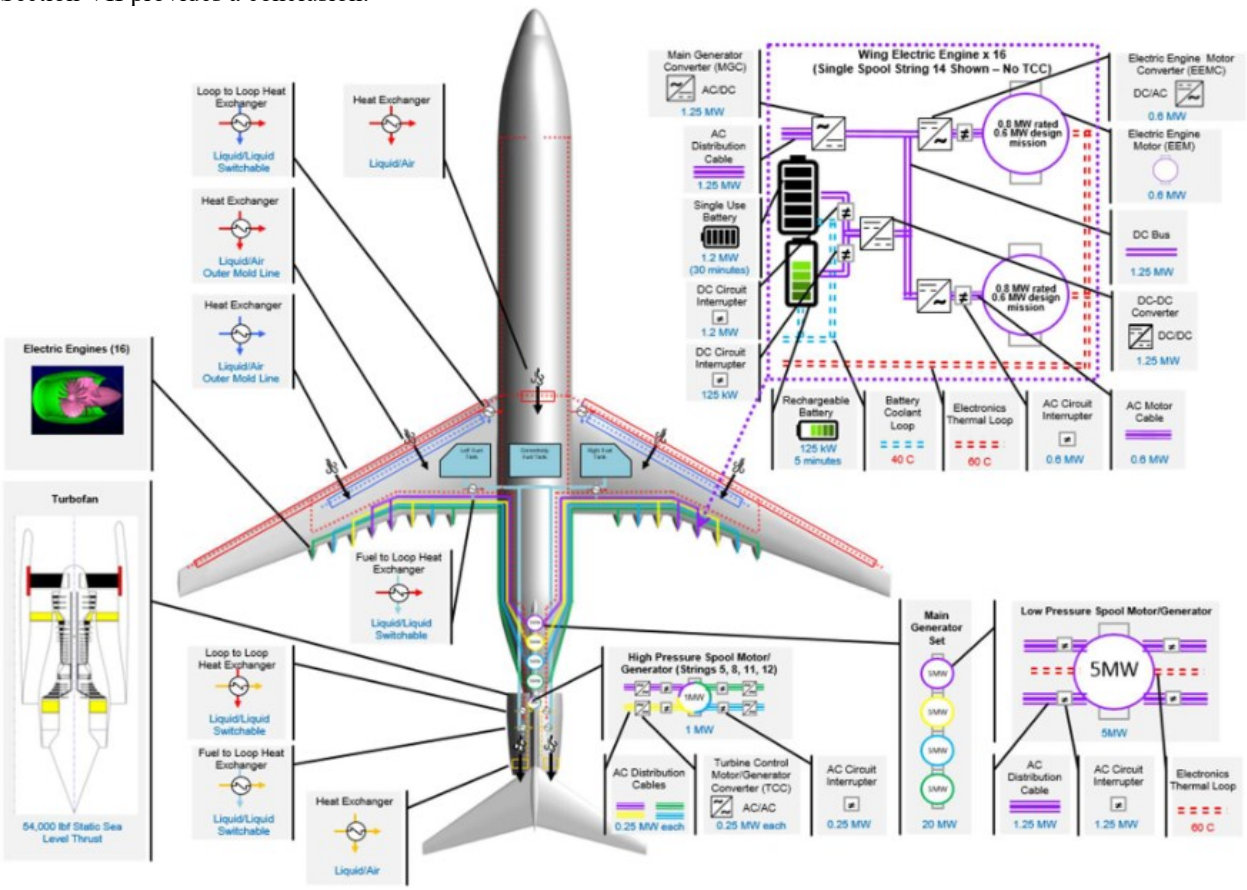

Fig. 1 Propulsion system layout for SUSAN electrofan [4].

II. Machine Design Requirements and Assumptions

Table 1 provides the top-level requirements and assumptions for the 5MW machine design. The bulk of the requirements and assumptions match what was assumed for the radial-flux machine designed in [5]. One notable difference in the assumptions is the selection of the potting compound for the stator windings. A higher thermal conductivity but lower thermal class epoxy is assumed. Initial winding lifetime aging results in [15] suggest that this epoxy, despite its lower listed thermal class, has better lifetime than the epoxy used in HEMM.

Table 1 Top level performance targets and assumptions.

Efficiency	99 %	**Stator and Rotor Iron Material**	$Fe_{49.15}Co_{48.75}V_2$
Specific Power	25 kW/kg	**Stator Conductor Material**	Copper litz wire
Nominal Rotational Speed	5951 rpm	**Stator Strand Insulation**	MW-16 polyimide
Maximum Radius	0.5 m	**Stator Potting Epoxy Thermal Conductivity**	1.9 W/(m*K)
Rotor Type	Wound field	**Stator Cooling**	Direct liquid
Rotor Cooling	In-shaft cryocooler	**Coolant Inlet Temperature**	60 ˚C
Rotor Conductor	2G high temperature superconductor (REBCO)	**Maximum Allowable Stator Temperature**	180 ˚C
Rotor Coil Fill	90%	**Coolant**	PAO

The assumed cryocooler performance is the same as was used for the radial-flux machine in [5]. Figure 2 shows the assumed cryocooler lift and required input power versus cold tip temperature. The cryocooler mass is assumed to be 35 kg.

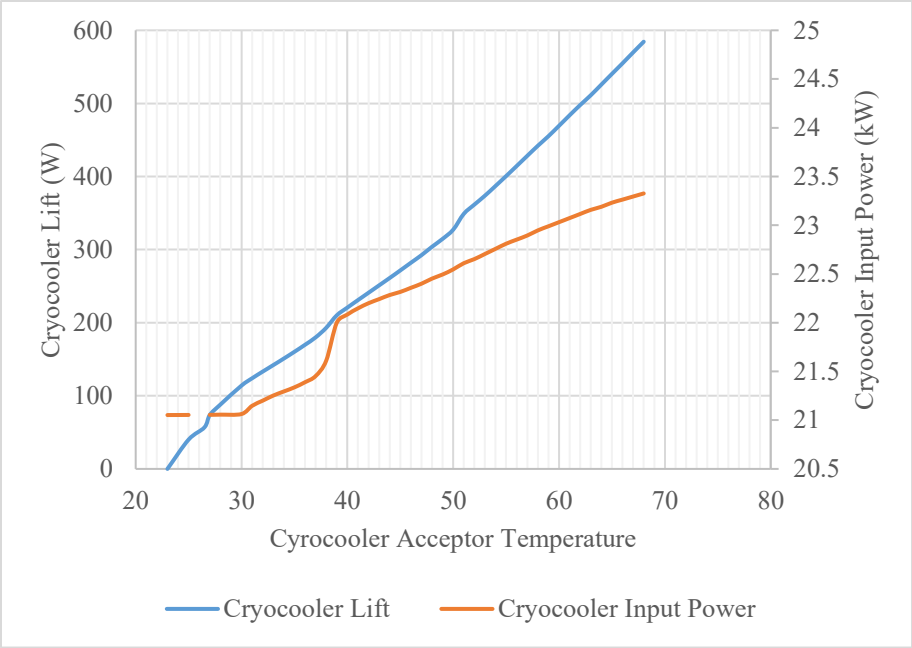

Fig. 2 Assumed cryocooler performance for concept machine design.

Appendix A provides graphics of the various machine topologies studied in this paper. Basic descriptions of each topology are provided below. Each listed topology is considered both with and without a rotating vacuum tube and eddy current shield around the rotor. In every case, the rotor is operated in a sufficient vacuum to eliminate convective heating of the rotor. The combined rotating vacuum tube and eddy current shield eliminates (a) rotor eddy current losses on the cryogenic components and (b) vacuum seals installed at the rotor-to-stator interface (i.e., rotary vacuum seals), which incur frictional loss and wear and are more prone to leaks than stationary seals. However, the rotating vacuum tube and shield introduces windage loss on the outside of the vacuum tube and enlarges the magnetic gap between the rotor and stator by 3-5 mm depending on the size of its structure. A loss of 2 kW is added to all designs with rotary seals instead of a rotating vacuum tube. Elimination of the eddy current shield imposes added requirements to the generator's power electronics to maintain nearly perfect sinusoidal current waveform in the machine; this is discussed in [16] and [17] along with a feasible converter design that produces little to no eddy current loss in the HEMM rotor. Those converter predictions assumed a perfectly stiff DC bus voltage, which may underpredict the rotor loss that occurs with a more realistic flight-weight aircraft bus. A rotor heat load of 15 W is added to all designs without an eddy current shield to account for eddy current losses on the rotor.

A. Baseline Axial-Flux Topology

This topology is an air-core, axial configuration with two stators and one rotor. The rotor is cooled at its inner diameter by a thermal bridge that connects it to the cryocooler's cold head. A stator is located on each axial side of the rotor so that field from both sides of the superconducting coils is used to produce torque. The stators are directly liquid cooled by fluid flowing around the stator windings and their support structure. The fluid is contained by a ceramic structure around each stator. Two rotating iron annuluses positioned axially outboard of the stators provide a return path for the magnetic flux and prevent leakage out of the axial ends of the machine. The disks rotate with the rotor so that no iron loss occurs in them at the fundamental electrical frequency.

A closed solution for the baseline design could not be found at this time due to difficulties making electrical connections on the rotor and rotor cooling. With this topology, rotor current lead connections would have to be made on the outside of the coils, creating breaks in the coil fixture. As discussed in [5], air-core superconducting coils operate in high self-field and correspondingly require significant external mechanical support to react the outward pressure created by the interaction of the coils' self-field with its current. Electrical connections on the outside of the coil make mechanical support challenging. Cooling of the superconducting coils is also difficult with this topology as

the thermal bridge can only make a connection with the inner diameter of the rotor. Thus, the cooling occurs through multiple thermal interfaces and is dependent on the thermal conductivity of the conductor and surrounding support structure.

The baseline design is included in this paper as a reference for the reduction in magnetic performance that results from the mid-bridge designs discussed in Sections II.B and II.C, which solve the rotor coil thermal and electrical connection issues.

B. Single-Stack, Mid-Bridge, Axial-Flux Topology

The topology matches the baseline axial design except that the thermal bridge extends radially through the middle of the superconducting rotor, separating the superconducting coils into two halves. The thermal bridge is also used as the coil-to-coil current jumpers, as was done for the radial topology in [5]. This mid-bridge design allows the coils' current connections to be made on the interior surface of the coils without interrupting the mechanical support on the outside surface. The bridge and current connections provide a good thermally-conductive path through the rotor. The addition of the bridge into the middle of the rotor creates a large magnetic gap between the two halves of the superconducting coils, reducing flux in the stator windings at a given rotor current. To keep current lead connections between coils on the inner surface of the coil, the number of coil layers must be a multiple of 4.

Two stator topologies, shown in Fig. 3 and Fig. 4, are considered for the mid-bridge topology machine. The first (Fig. 3) is termed here the "distributed" topology. It has no winding skew in the active region of the machine. Hence, it has large, complex end windings that span the arc between slots of the same phase. The second (Fig. 4) is termed here the "zig-zag" stator topology. It has skew close to one full pole pitch and minimal end-winding length. The zig-zag stator has a two-layer construction with a non-metallic support structure between the front and back layer. This non-metallic support structure creates an additional 2 mm magnetic airgap to the axially outboard winding layer. The skew additionally reduces torque per ampere in a given slot relative to the distributed topology.

Fig. 3 "Distributed" stator topology. Windings have no skew in the active region of the machine and correspondingly complex end turn geometry.

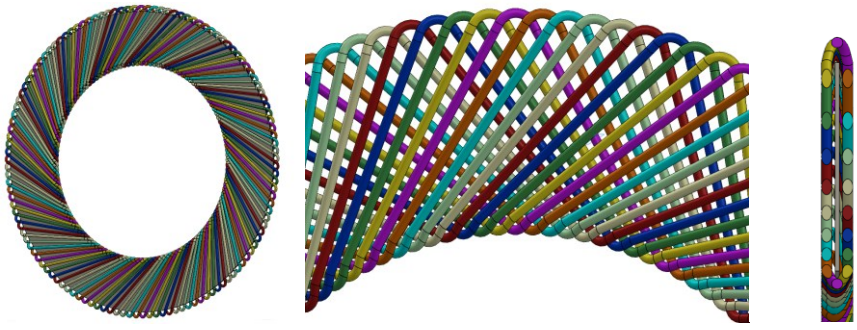

Fig. 4 "Zig-Zag" stator topology. Windings are skewed by approximately one pole arc in the active region of the machine in order to minimize end winding complexity and mass at the cost of reduced torque production due to the winding skew.

C. Multi-Stack, Mid-Bridge, Axial-Flux Topology

The topology matches the single-stack, mid-bridge one but with more than one superconducting rotor and correspondingly three or more stators. This topology requires the use of the zig-zag stator topology for the stators

located between the rotors, because the end windings of the distributed topology would result an excessively large gaps between rotors. This topology is only considered without a rotating vacuum tube because of the mechanical complexity that would be required to create a sealed vacuum tube around each rotor without contacting either the rotors or the stators of the machine. In this paper, a zig-zag type is used for every stator in this topology. However, it is feasible to use a distributed type for the two axially outboard stators and a zig-zag type for the remainder.

D. Radial-Flux, Air-Core Topology

This is the same topology as the concept design in [5]. The rotor is air-core and the stator back-iron is placed at a distance radially outward of the machine. One of the major omissions in the design tool's mass prediction for the design in [5] was the rotor's mechanical mass. As is shown in Fig. 29, the rotor structure has been updated to account for the additional mass and required stainless steel components for the rotor's structural design.

E. Radial-Flux, Iron-Core Topology

This topology matches that of the HEMM motor. An iron core rotor and a close fitting back-iron is used in the machine electromagnetic geometry.

III. Design Tool

The design tool in this paper is an updated version of the partially superconducting design tool used in [5]. The subsequent sections discuss the adaptation of the design tool for the axial flux machine topology and other updates made to the design tool to account for lessons learned in [5]. A flow chart of the design tool is depicted in Fig. 5.

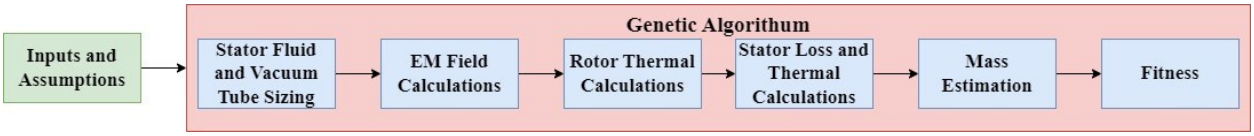

Fig. 5 Flow diagram of design tool.

A. Stator Fluid Containment Tube and Vacuum Tube Sizing

The vacuum tube and stator fluid containment structure of all designs are in the airgap of the machines, between the stator and rotor coils. Correspondingly, their size contributes to the magnetic gap in the machine. The stator fluid containment and vacuum tube sizing assumptions from [5] are maintained for all radial designs. Buckling of thin-walled cylinders is used to estimate the required thickness of both tubes.

For the axial designs, simple estimates of component thicknesses are used. The stator fluid containment tube is assumed to be 1.5 mm thick and made of alumina. The vacuum tube/eddy current shield is assumed to be made of 2 mm thick copper. An additional 1.5 mm-thick end wall on the rotor structure is also included in the airgap of the machine. Thus, the total airgap between the rotor and stator coils for an axial design with a rotating vacuum tube is 7 mm plus the thickness of the fluid cooling channel on the axial face of each stator (typically 1 mm).

B. Electromagnetic Field Calculations

For the radial, iron-core topologies, magnetic field calculations are carried out with the method described in [7]. For radial, air-core designs, field calculations are caried out using the Biot-Savart Law as described in [5].

For the axial designs, a 2D planar representation of a cylindrical slice through the motor's electromagnetic geometry is used to estimate the fields created in different components. A slice at the inner active radius of the machine is used to calculate the rotor's critical current. Field calculations are carried out at multiple locations in each layer of the superconducting coil by summing the field produced by each coil turn calculated using the Biot-Savart Law. An iterative solver is used to select the rotor current that results in critical current being 1.5 times the rotor current, like in [6].

Stator field calculations are carried out using a slice of the magnetic geometry at the mean magnetic radius of the machine. Three poles of the rotor are modeled and used to calculate the field on one pole worth of stator coils. The magnetic field is calculated at 9 points within each stator coil by summing the field produced by every rotor turn calculated using the Biot-Savart Law. The field is then used to back-calculate the required stator current to achieve the desired torque.

Field in the rotor iron is estimated by calculating the flux density just outside of the iron at the center of a rotor pole using the Biot-Savart Law. The calculated field value is assumed to be the peak value of a sinusoidal distribution such that the required iron thickness t_{iron} to keep the flux density of the iron below saturation is calculated as

$$t_{iron} = B_{iron} * \frac{2}{\pi} * \frac{L_{Rotor_{Pole}}}{B_{sat}},$$

where B_{iron} the field calculated at the surface of the iron, $L_{Rotor_{Pole}}$ is the width of the stator pole, and B_{sat} is the saturation inductance of the iron (assumed to be 2 T).

C. Cryocooler Heat Load and Power

Cryocooler heat load for all designs is quantified as the sum of estimated radiation heat transfer, heat leak through the current lead wires, heat leak through mechanical components, and heat generated in the rotor. The radiation heat load to the rotor is calculated as

$$Q_{rad} = \sigma * A_{rotor} * \frac{T_H^4 - T_{coils}^4}{\frac{1}{\varepsilon_{rotor}} + \frac{1}{\varepsilon_{vacuum}} - 1}$$

Where Q_{rad} is the heat load due to radiation, σ is the Stefan-Boltzmann constant, A_{rotor} is the rotor surface area, T_H is the temperature of the surrounding components estimated at the temperature of the cooling fluid (60 °C), T_{coils} is the operating temperature of the coils, ε_{rotor} is the rotor's emissivity (assumed to be 0.02 for gold plating), and ε_{vacuum} is the emissivity of the vacuum tube (taken to be 0.13). The low emissivity assumed for gold plating is based on small sample tests completed for the design of the HEMM rotor [12]; however, recent cryogenic testing of the HEMM rotor suggest that achieving and sustaining this low emissivity over the entirety of a complex rotor structure may be difficult [18] [19] [20].

The heat leak along the rotor current lead wires that carry current to the rotor superconducting coils is estimated based on lead wire optimizations presented in Appendix B of this paper. The results of the optimization showed a linear relationship between heat leak and rotor current as described by the equation

$$Q_{lead} = 0.1066 * I_{rotor},$$

where Q_{lead} is the lead heat load to the cryocooler and I_{rotor} is the rotor current. As described in Appendix B, this heat leak estimate is made for a cryocooler cold head temperature of 26 K (a conservative lower bound in this paper) and a current lead hot end temperature of 353 K.

Heat leak into the rotor from the mechanical connection to the shaft and other sources is estimated as

$$Q_{mechanical} = 25\ W.$$

Heat generated in the cryogenic rotor is estimated as

$$Q_{loss} = \begin{cases} 0\ W, \text{with an eddy current shield} \\ 15\ W, \text{no eddy current shield} \end{cases},$$

based on scaling the eddy current loss estimates in [17] for the HEMM rotor to the power level considered here. The total heat load to the cryocooler $Q_{cryocooler}$ is

$$Q_{cryocooler} = Q_{lead} + Q_{rad} + Q_{mechanical} + Q_{loss}.$$

The required temperature of the cryocooler to maintain the target coil temperature is estimated as

$$T_{cryo} = T_{coil} - \frac{2 * Q_{cryocooler}}{k_{bridge} \frac{2\pi * R_{shaft} * t_{bridge}}{R_{rotor} - R_{shaft}}}$$

where T_{cryo} and T_{coil} are the temperature of the cryocooler and coil, respectively, k_{bridge} is the thermal bridge's thermal conductivity (estimated at 350 W/m-K), R_{rotor} is the rotor's radius, and R_{shaft} is the shaft's radius (estimated as 0.06 m). The thermal bridge's mass $Mass_{bridge}$ for radial designs is estimated as

$$Mass_{bridge} = 4 * D_{copper} * t_{bridge} * \pi * R_{shaft} * \sqrt{\left(\frac{Stack}{2}\right)^2 + \left(R_{rotor} - R_{shaft}\right)^2},$$

where D_{copper} is the density of copper and $Stack$ is the active axial length of the rotor. This estimate accounts for the lesson learned in [5] that the bridge must make thermal connections to the axial ends of the rotor to achieve good thermal performance in the rotor end windings. For axial designs, the thermal bridge's mass is estimated as

$$Mass_{bridge} = 3 * D_{copper} * t_{bridge} * \pi * R_{shaft} * \left(R_{rotor} - R_{shaft}\right).$$

The heat lift of the cryocooler at the estimated cryocooler temperature is modeled using the cryocooler performance estimates in Fig. 2. If the lift is less than $Q_{cryocooler}$ for a given design, the design is assigned a low fitness value in the genetic algorithm. When the lift is greater than or equal to $Q_{cryocooler}$, the rotor design is assumed to be thermally feasible. The cryocooler's input power is estimated using the data in Fig. 2 and included in the efficiency estimate for the machine.

D. Losses and Efficiency

Stator losses and thermal performance of the radial topologies is completed using the method described in [7]. No iteration of thermal analysis and winding design are completed in this paper since the assumed stator winding temperature for initial loss calculations is close to the temperature limit for the epoxy. Not iterating the thermal and loss calculations leads to an underprediction of efficiency for designs that operate colder than the assumed conductor temperature.

The axial design tool uses axial adaptations of the radial stator loss and stator thermal performance models. Stator AC resistive and proximity losses are calculated for all possible combinations of wire gauge and winding turn count. The winding design that minimizes total losses is then selected and thermal analysis is completed for that design. Each set of stator windings has a separate cooling loop in which fluid enters the stator fluid containment cavity near the outside diameter, flows radially inward along one axial face of the machine, past the end windings closer to the axis of rotation, radially outward along the other axial face of the winding, along the outer end windings and exits the machine again near the outer diameter. Due to the varying cross-sectional area of the flow path as the fluid goes from inner to outer diameter of the machine, no explicit Nusselt number correlation is readily available. As a conservative estimate of the flow cooling performance, only laminar flow is considered and a Nusselt number of 3.66 is assumed for all convection calculations.

A 1-dimensional thermal model from the front axial face of the machine to its outer axial face is used to obtain an estimate of the stator conductor's temperature. A reluctance network consisting of 10 elements was used to discretize the stator windings axially. The cross-sectional area of each element is assumed to be equal to the annulus spanned by the inner and outer winding radii. No attempt is made to account for the surface area added by the end winding's out-of-plane bending. The winding's thermal conductivity in each element of the reluctance network is estimated using the rule of mixtures and typically falls in the range of 3-5 W/mK using the assumed high-thermal-conductivity epoxy in this paper.

As will be shown in Section IV-C-2, the thermal model used for axial designs is an identified area of refinement for future design tool iterations since the predicted stator coil temperature was estimated to be significantly above that predicted by a higher-fidelity model. The low-fidelity model with assumed laminar flow is conservative and leads to an underestimate of the axial flux machine's achievable specific power.

Efficiency is calculated accounting for stator winding loss, stator iron loss, cryocooler power, windage losses (when present), current lead losses, fluid flow pumping power, and seal losses (when present).

E. Mass Estimate

The calculated mass of each machine includes the mass of the magnetic components, the cryocooler, and an estimate for the structural components. For all machines, the rotor coil support is assumed to be constructed of 316 stainless steel. The remaining bulk of the rotor structure is assumed to be constructed of Ti. The eddy current shield is assumed to be supported by a titanium structure for all topologies. The stator winding support structure is assumed to be made of fiber reinforced plastic. Stator fluid containment tubes are assumed to be constructed of alumina. The outer housing's mass is estimated by calculating the mass of a 4 mm thick aluminum cylinder that encompasses the machine.

F. Fitness Definition

The genetic optimization algorithm uses a multi-element array to define fitness, and two elements are used in this study. If the design closes thermally, the elements are specific power and efficiency. If a machine doesn't close thermally and has a specific power less than 30 kW/kg, the elements are its specific power and the reciprocal of its predicted winding temperature. If a design has a specific power greater than 30 kW/kg both fitness variables are set equal to zero. With this method, designs that do close thermally are optimized for improved specific power and efficiency while designs that have specific powered greater than designs that have closed thermally are optimized for improved thermal performance.

IV. Design Study Results

The design tool was exercised for every topology described in Section II. The following subsections discuss the results of the axial machine, the radial, air-core machine, and the radial, iron-core machine, followed by a comparison of the three.

A. Axial-Flux Topology Trade Study Results

Fig. 6 shows the complete results for the axial topologies. Fig. 7 shows a zoomed in view of the results around 99% efficiency and 20 kW/kg. Fig. 8 shows the superconductor operating temperature vs efficiency for all designs.

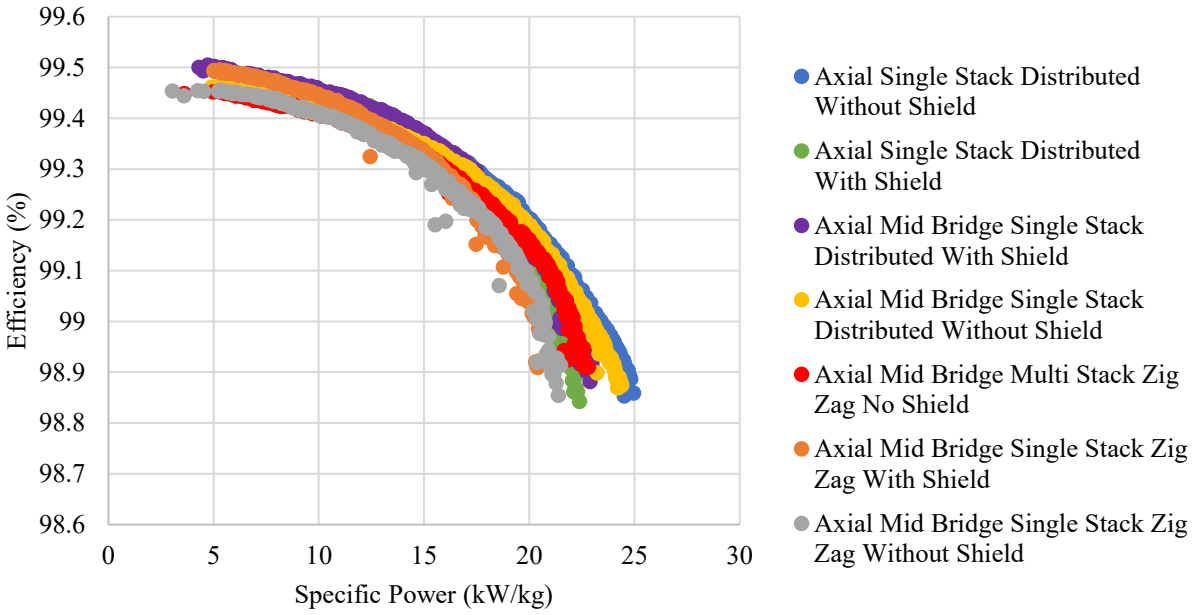

Fig. 6 Axial flux topology results from design tool.

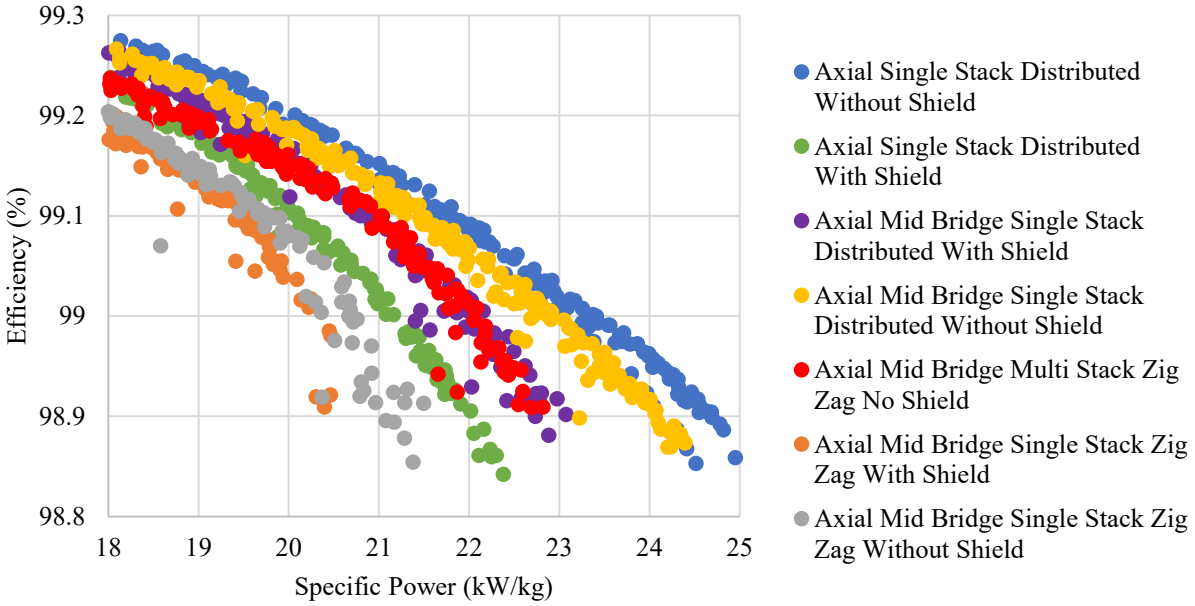

Fig. 7 Zoomed in view of axial machine trade space focusing on region around 99% efficiency and 20 kW/kg.

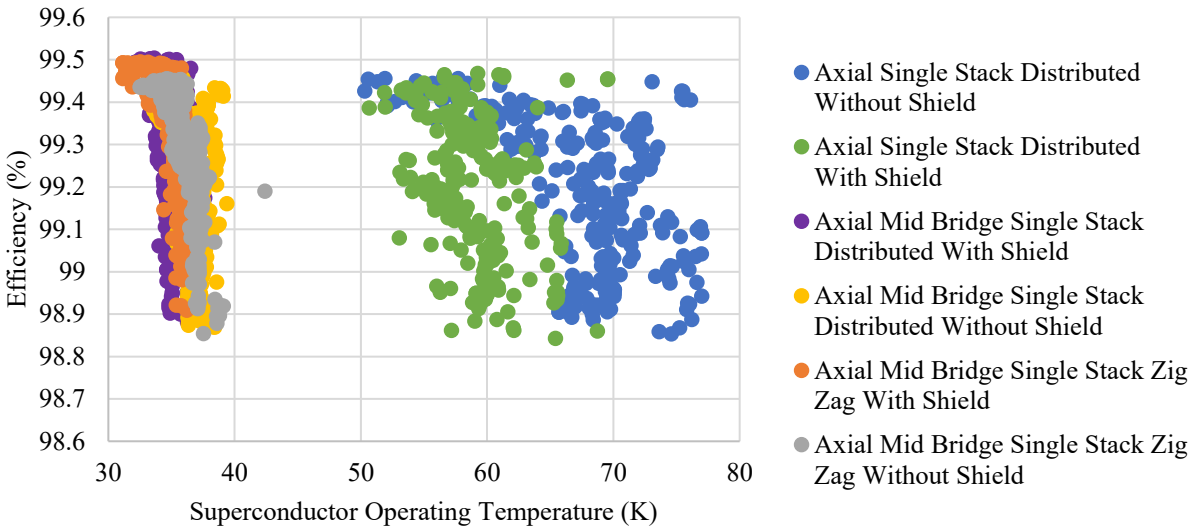

Fig. 8 Axial machine topologies superconductor temperature versus efficiency.

For all axial topologies, the variant without a rotating vacuum tube and eddy current shield outperformed the variant with one. The 15 W of assumed eddy current loss on the un-shielded variants only led to a 1-3 K increase in the superconductor's operating temperature due to the assumed cryocooler performance increasing significantly with temperature in Fig. 2. Hence, the reduced airgap, mass, and windage loss from not having the rotating vacuum tube and eddy current shield outweighed the rotary seal loss and increase in the superconductor's operating temperature. The assumed 15 W is a rough approximation of eddy current loss that puts significant burden on the power electronics to provide nearly perfect sinusoidal waveforms to the stator windings. Once the power electronics are modeled, the system-level trade between having or not having a shield should be revisited. Design studies exploring sensitivity of performance to the estimated rotor eddy current loss could be valuable for defining this trade.

The distributed winding topology is shown to outperform the zig-zag stator topology despite the larger end-winding length. The reduction in active region torque with the skewed winding and the added airgap between winding layers was significant enough to outweigh the reduced end winding length relative to the distributed topology. The end-winding length for most of the distributed windings was roughly equal to the machine's active length. The multi-stack topology with zig-zag stator does show some performance improvement relative to the single stack topology with zig-zag stator, but the benefit is not sufficient to make it competitive with distributed topologies and outweigh the added complexity.

The axial, single-stack machine without the mid-bridge is seen in Fig. 6 and Fig. 7 to outperform the topologies with the bridge. As shown in Fig. 8, the topologies without the bridge have their superconductors operating at a much higher temperature (and thus significantly reduced current densities) than the topologies with the bridge due to the higher thermal resistance between the conductor and the cold head of the cryocooler. This higher temperature is found to be fully offset by the elimination of the airgap created by the bridge, which typically optimized to about 2 cm thick for topologies with a mid-bridge and contributed significantly to the total magnetic gap of the machines. However, as noted in Section II.A, the axial machine without mid-bridge does not have a closed mechanical solution. Thus, the axial topology with a bridge is selected for FEA refinement in Section V.

Overall, the results can be summarized as generally favoring topologies that minimized the required stator current density by having lower conductor temperatures, smaller effective magnetic gaps between the rotor coils and the stator coils (with vs without shielding), or minimizing stator slot skew (zig-zag vs distributed). The bulk of the losses for all machines are the cryocooler loss and the stator resistive losses. Per Fig. 2, there is minimal variation in cryocooler power for the assumed cryocooler in this study and typically falls around 20-21 kW. As a result, in-order to achieve >99% efficiency, the optimization focuses on minimizing resistive losses in the stator to around 25 kW. If a different cryocooler performance versus temperature was assumed, the above trade space results may favor a different topology of machine.

B. Radial-Flux, Air-core Topology Trade Space Results

The results for the air-core radial topology are shown in Fig. 9. For the air-core radial topology, removing the rotary shield and vacuum tube from the designs again results in a predicted improvement in machine performance but as mentioned previously leads to implementation challenges and adds additional constraints to the power electronics design for the machine. The predicted performance for the air-core topologies with shields (22-24 kW/kg at 99% efficiency) is in good agreement with the estimated performance of the air-core concept design in [5].

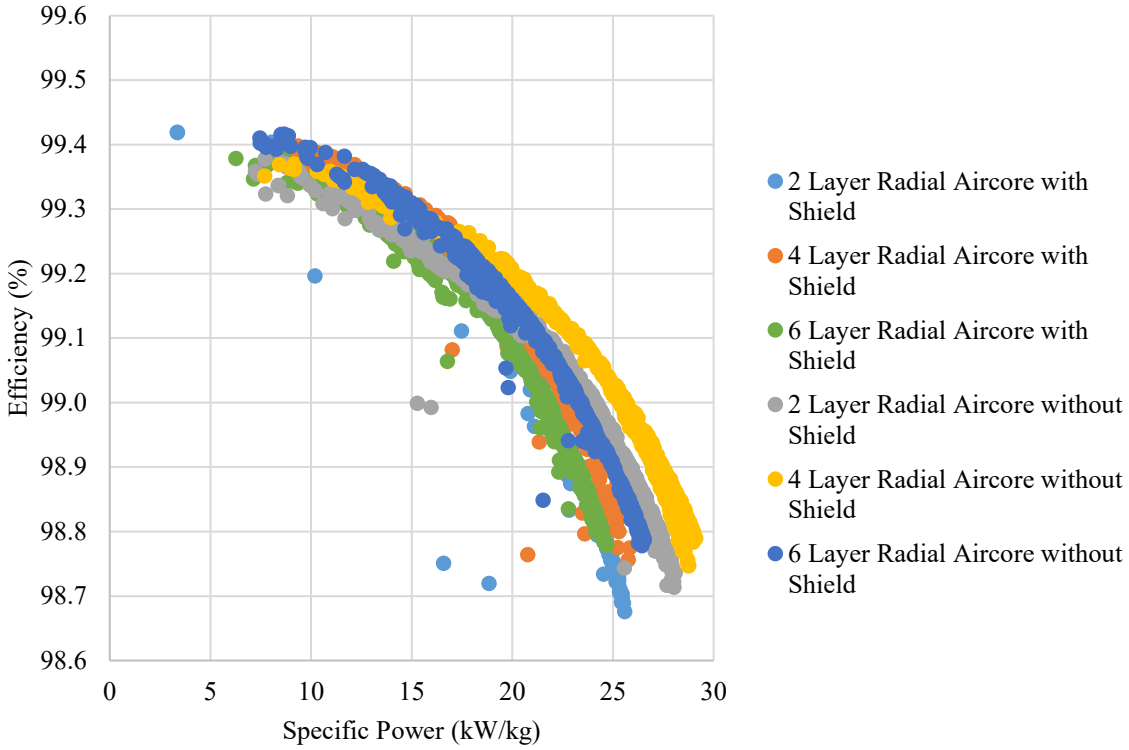

Fig. 9 Air-core radial topology results from design tool.

Compared to the results in [5], the results here exhibit a larger difference between topologies with 2- and 4-layer superconducting coils. This results from the 2-layer topologies' superconducting coils operating at higher temperatures than their 4-layer counterparts due to this study's inclusion of the lead wire losses in the cryogenic heat load for the rotor. Fig. 10 shows the superconductor temperature for all 2- and 4-layer designs versus temperature. Four-layer designs are shown to operate 1 to 2 K colder than their 2-layer counterpart. To achieve the same total Amp-turns around a rotor pole in the 2-layer topology, a higher supply current is required than what is required for the 4-layer topology. Correspondingly the 2-layer topologies have higher lead losses and higher temperatures.

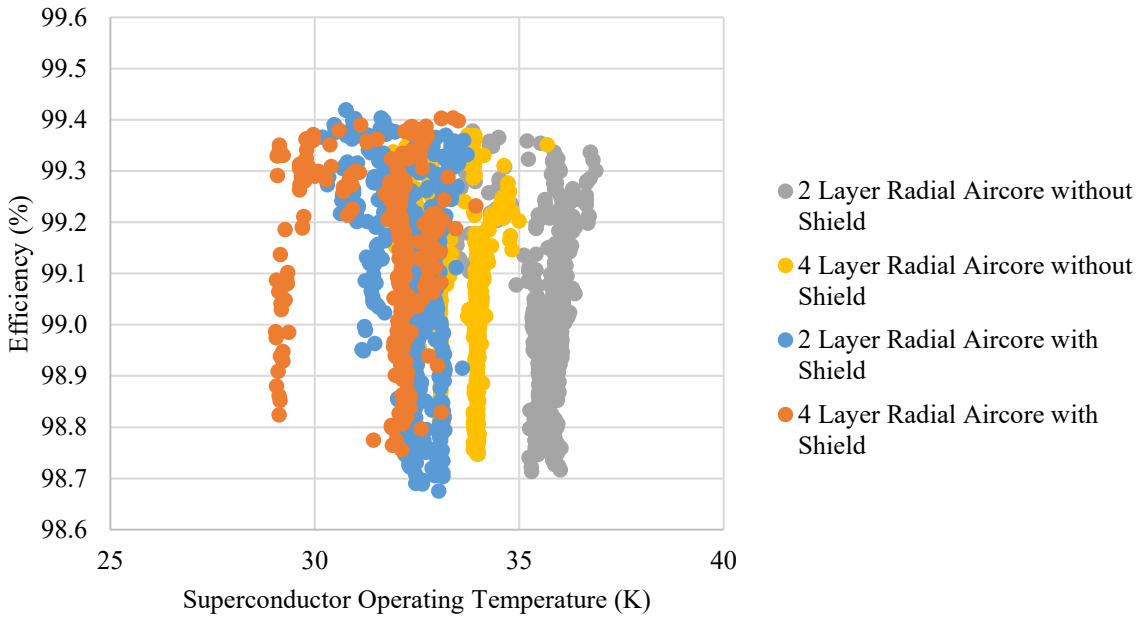

Fig. 10 Efficiency versus superconductor temperature for radial air-core results.

C. Radial-Flux, Iron-Core Topology Results

Results for the iron-core radial topologies are shown in Fig. 11. Iron-core designs are shown to have the lowest performance of all the machine topologies studied. The appreciable loss and mass of these designs' close-fitting back iron on the stator is not sufficiently compensated for by an improved magnetic circuit. As noted in [5], these designs have higher power density than their air-core counterparts, and although they are not able to achieve the target machine performance for this application, they may become the best solution in a more volumetrically constrained design problem.

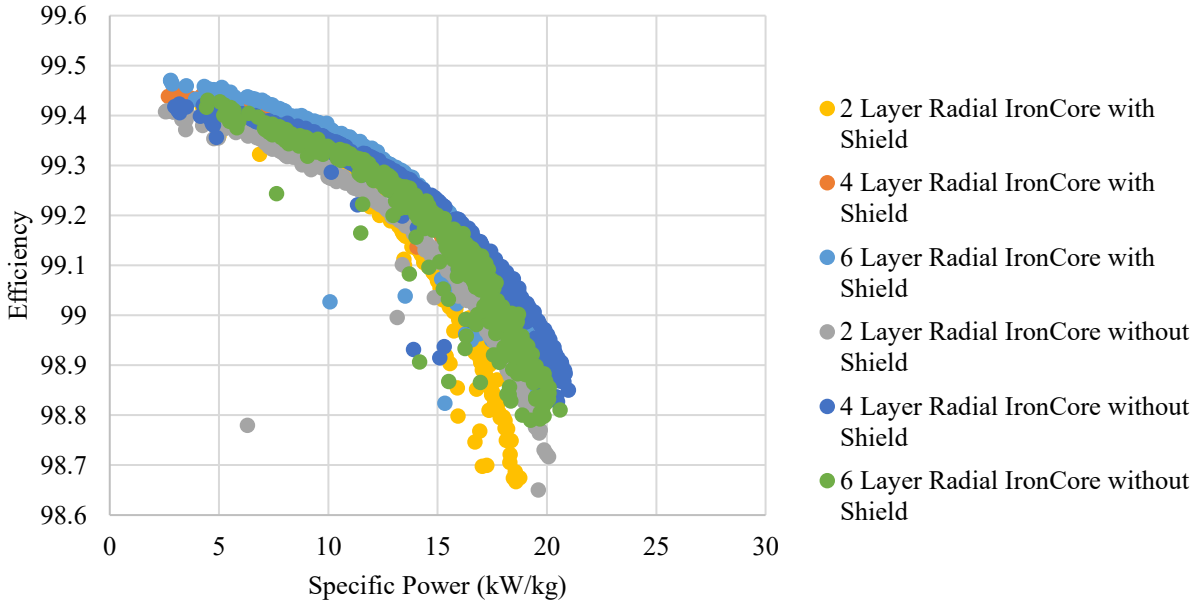

Fig. 11 Iron-core radial topology results from design tool.

D. Comparison of Candidate Machine Topologies

Fig. 12 shows a comparison of the different topologies. As noted previously, iron-core designs underperform relative to the air-core and axial topologies. The 4-layer radial, air-core topology without an eddy current shield is predicted to be able to meet the target specification for the SUSAN application at 99% efficiency and 25 kW/kg. The axial topologies are predicted to not meet the target specification with this iteration of the design tool. Axial designs outperform radial ones below 19 kW/kg but exhibit a steeper decline in efficiency as specific power increases above that value. This trend may result from the low fidelity nature of the axial machines' thermal model used in this iteration of the design tool. As is shown later in the detailed design, the tool significantly underpredicts thermal performance relative to axisymmetric FEA. However, the refined mass prediction exceeds that determined by the tool. The design tool for axial-flux machines will be refined in future work to increase the fidelity of the thermal analysis to the level currently in place for the radial, air-core design and described in [5].

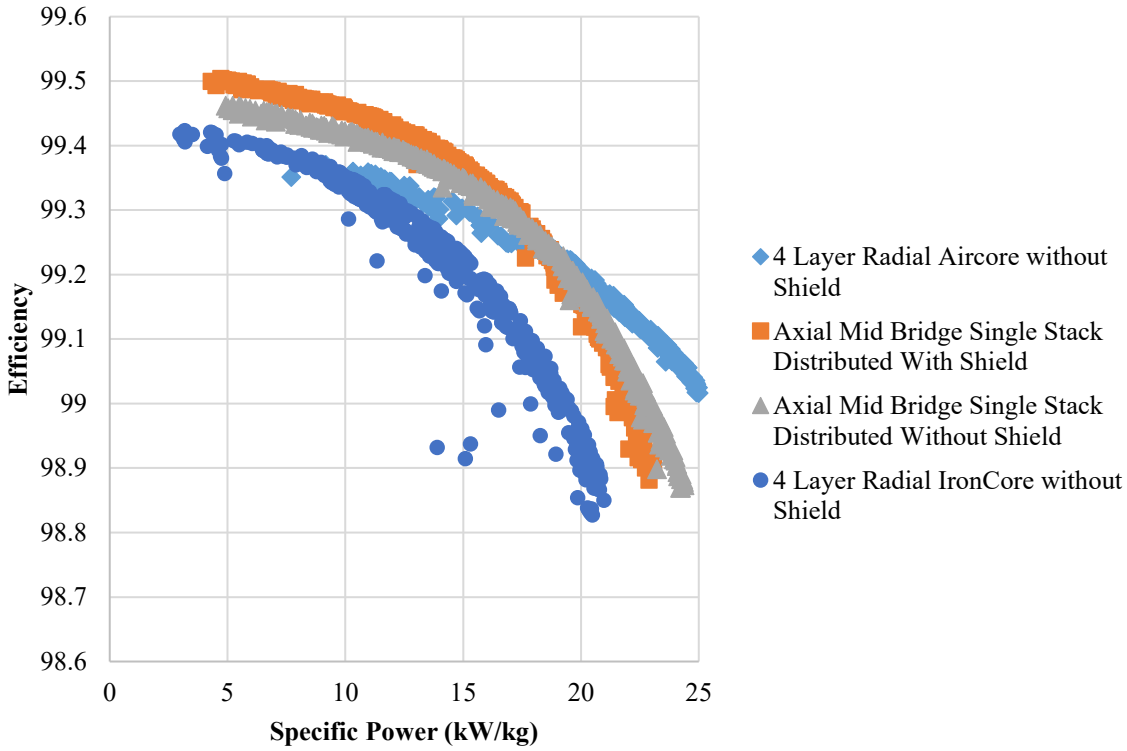

Fig. 12 Comparison of best designs from different topology studies.

V. 2D FEA Design Refinement

To refine the analytical design tool's results and improve accuracy prior to selecting a design, a secondary optimization was completed for two axial design topologies. For this secondary optimization, 2D FEA magnetic analysis was added to the end of the design tool to increase its accuracy. If a design made it through all steps of the analytical tool and had sufficient fitness to be a candidate design, the 2D FEA model was first run to improve the accuracy of the critical current prediction and then to refine the required stator current. The geometry of this model is shown in Fig. 13.

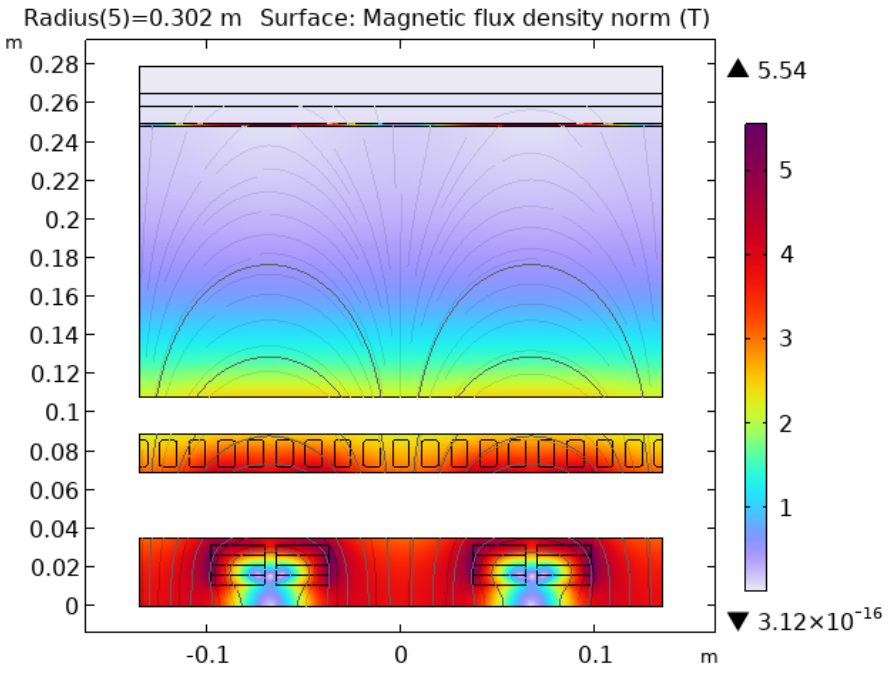

Fig. 13 Geometry and example result from 2D electromagnetic FEA model of an axial machine.

The refinement of critical current (and thus superconductor operating current) was completed using a 2D representation of the motor's magnetic geometry at the inner magnetic radius. Prediction of the required stator current was completed by running 2D torque calculations at 5 different radii spanning the inner to outer active radius of the machine; this required 5 separate FEA simulations, which each used the analytically-predicted required stator current and the updated superconductor operating current. Required current was then increased proportional to the difference between required torque and FEA-predicted torque. Losses were re-calculated, and an analytical thermal analysis was completed to ensure the design still closed.

The FEA-based design refinement was completed for axial mid-bridge topologies with distributed stators, both with and without rotating vacuum tubes. Fig. 14 shows the results of both optimizations. The topology without the rotating vacuum tube is shown to maintain a minor improvement in achievable specific power at 99% efficiency relative to the topology with the rotating vacuum tube due to the smaller magnetic gap in the machine. The topology without the shield is predicted to have its superconductor operate 3-4 K hotter than the one with a shield. As mentioned previously however, this relative performance is with an assumed eddy current loss of 15 W on the rotor, and that is only valid if the power electronics maintain nearly perfect sinusoidal waveforms in the machine's stator.

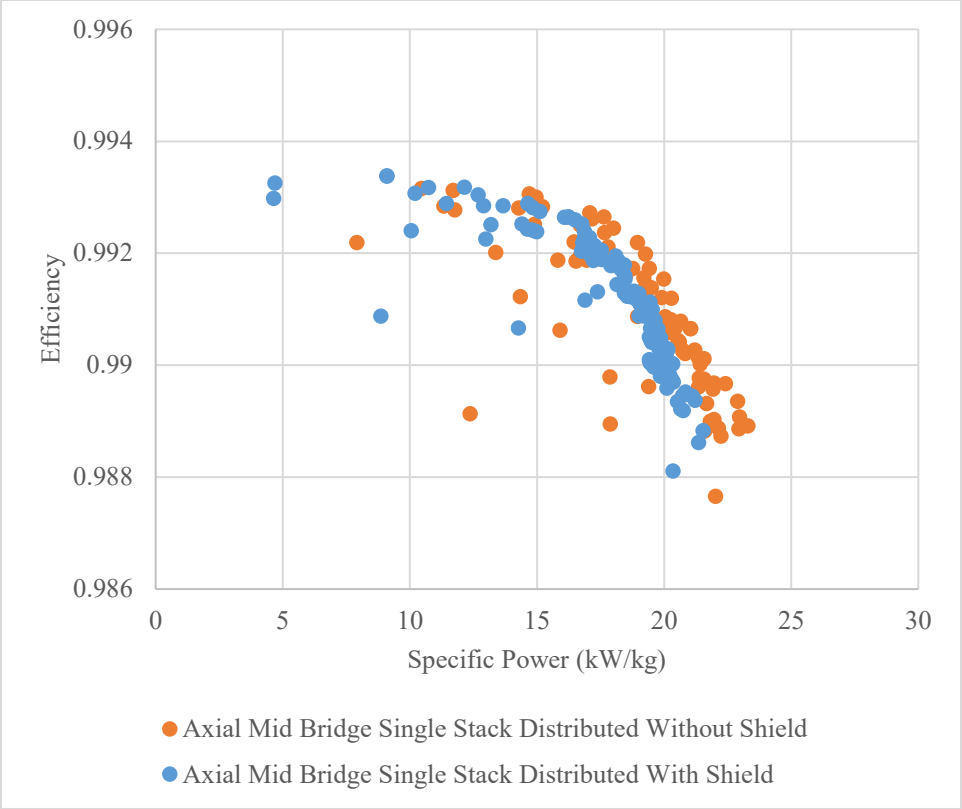

Fig. 14 Results of 2D FEA refinement of axial flux topologies.

Fig. 15 shows the FEA results compared to the analytical predictions. A 1-2 kW/kg reduction in achievable specific torque is predicted by the FEA results relative to the analytical prediction.

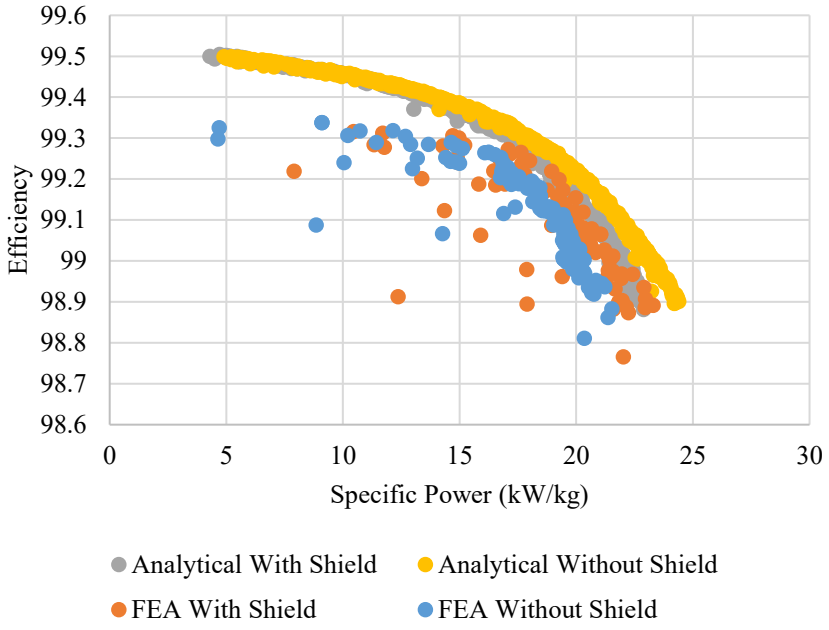

Fig. 15 Comparison of FEA and analytical performance predictions for axial flux machines.

VI. Concept Design

From the 2D-based FEA optimization, a design without shield was selected for further refinement. Table 2 provides the key dimensions and performance parameters for the design as predicted by the refined design tool. The following subsections show higher fidelity magnetic, mechanical, and thermal models. These models are used to assess the accuracy of the design tool's performance predictions so that updates can be made to the tool's assumptions before the next design iteration.

Table 2 Selected design dimensions and performance predictions from the design tool.

Top Level		**Currents**	**A**
Rotor Pole Pairs	7	SC Critical Current	223
Stator Slots	126	Rotor DC Current	145
Power	5 MW	Current Per Stator Slot (rms)	613
Rotational speed	5,951 rpm		
Electrical Frequency	694 Hz		
SC Coil Layers	8	**Cryogenic Heat Loads**	**W**
		Rotor Radiation	10.4
Major Dimensions	**m**	Rotor Eddy Loss	15
Active Magnetic Outer Radius	0.302	Mechanical Heat Leak	25
Active Magnetic Inner Radius	0.2027	Rotor Lead Loss	15
Coil Width	0.0275	Total Rotor Heat	65.4
SC Tape Width	0.005	Cryocooler Lift	69.5
Winding Thickness	0.0134		
Thermal Bridge Thickness	0.022		
Iron Offset	0.15	**Temperatures**	**˚C**
		Cold Head	26.7
Mass	**kg**	Superconductor	37.6
Rotor Coil	67.1	Stator Hotspot	174
Rotor Mechanical	17.9		
Rotor Thermal Bridge	27		
Iron Rotors	11.2	**Losses**	**W**
Cryocooler	35	Fluid Flow Loss	93
Housing	22.23	Windage Loss	0
Stator Fluid Containment	4.5	Seal Loss	2,000
Stator Winding Mass	29	Stator Resistive Loss	26,814
Stator Structure Mass	20	Cryocooler Power	20,002
Total	233.93	Eddy Current Loss	633
Specific Power	21 kW/kg	Efficiency	99.01%

A. Higher-Fidelity Magnetic Analysis

According to the authors' previous work on radial machines [5] [6], 3D analysis of partially superconducting machines typically predicts a larger output power for the machine as flux in the end windings of both the stator and the rotor contribute a non-trivial amount of torque. 3D magnetic analysis was carried out for the selected axial machine concept design to assess how much additional torque is created by the end windings, update the critical current prediction for the rotor coils, and determine how far structural components would have to be separated from the rotor coils to avoid additional eddy current losses. Fig. 16 shows the geometry of the magnetic model. A section of the machine representing one axial half of one pole pair is simulated with symmetry conditions on the axial and angular cross-sectional faces of the geometry. A simplified representation of the stator windings with circular cross-section

and undersized diameter is used to simplify the geometry of the stator windings. Fig. 17 Figure 17 shows the applied current distribution in the rotor and stator coils. The non-uniform current density in the rotor coils results from parametric FEA representation of the rotor coil geometry that results in non-uniform cross-sectional area of the coil between the inner and outer end turns. The current concentrations in the rotor coils result from the low quality of the 3D mesh used in the rotor coils for this model iteration to make it practical to solve with available computing sources.

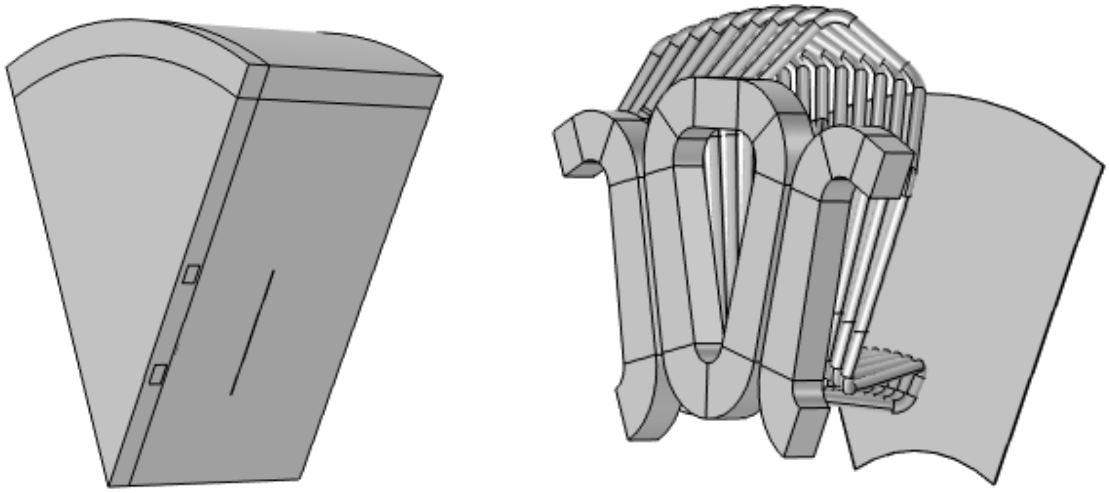

Fig. 16 3D Magnetic FEA simulation geometry. Left shows the overall geometry including air domains. Right shows the magnetic components (rotor coils, stator coils, and rotating back iron).

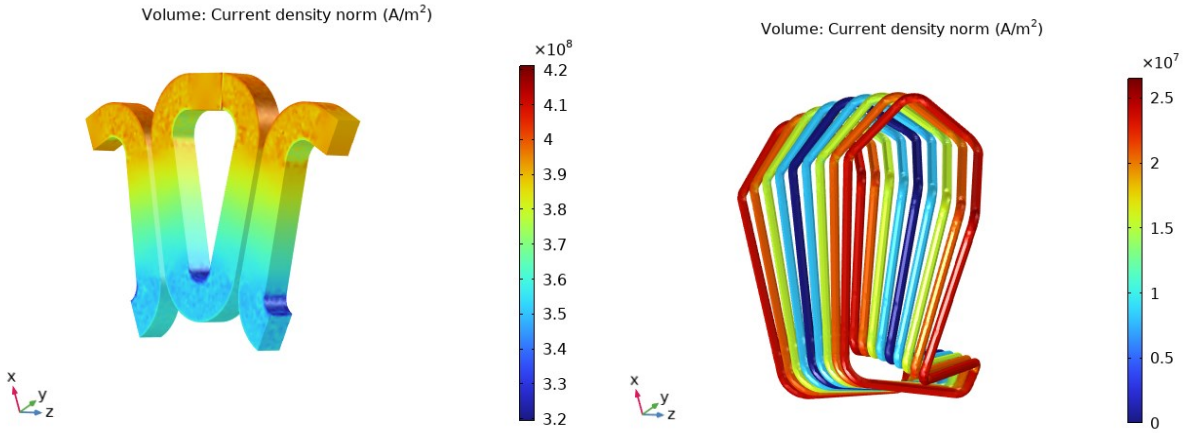

Fig. 17 Current density in both rotor coils (left) and stator coils (right) in the 3D magnetic model of the machine.

Figure 18Fig. 18 shows the magnetic field distribution in the stator and rotor coils. A maximum flux magnitude of 6.2 T is observed in the rotor coils, and a maximum axial field of 3.5 T is observed in the stator coils. Magnetic field data in the rotor coils from the simulation was extracted and used to predict the critical current in the coils. The resulting prediction was 237 A, which is approximately 14 A higher than the 2D FEA prediction; however, due to the coarseness of the mesh used in the 3D simulation, the accuracy of the prediction is only sufficient to verify the design. No increase in rotor current was applied for performance predictions.

The total predicted power using the torque calculated on the stator windings is 5.37 MW. The stator windings were used for torque prediction to avoid the sharp corners in the geometry of the rotor coils affecting the result. The added torque relative to the 2D prediction is contributed primarily by the end windings of the rotor coils. The end windings of the rotor coils produce comparable flux in the stator coils to the active region of the machine. On a percentage basis,

the added torque is less than the added length. The torque increase is similar to that observed for the radial machine in [5] where 5.46 MW was predicted with 3D FEA of that machine.

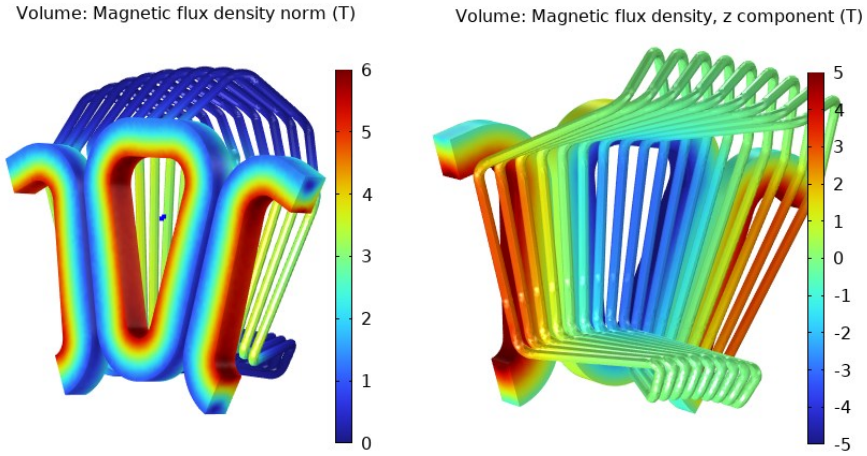

Fig. 18 Magnetic field predictions from 3D FEA simulation. Left shows flux density magnitude in both rotor and stator coils. Right shows only the axial (z-direction) component of the flux density.

Fig. 19 shows the flux leakage of the machine both on a linear scale and on a log scale. Significant radial 3D leakage is observable around the rotor end turns. Field levels above 0.1 and 0.01 T occur at radii of 0.4 and 0.5 meters, respectively. This leakage flux can generate significant losses in the housing of the machine and electromagnetic interference problems in nearby electronic circuits. Adding magnetic shielding at the outer diameter of the machine would reduce the leakage out of the machine at the costs of reduced torque (total leakage flux increases due to the leakage path's lower magnetic reluctance) and increased eddy current losses. The rotating iron has a visible effect in suppressing axial leakage flux. Further refinement of the size and position of these leakage disks could improve torque and reduce leakage but would require further 3D simulations of the machine. Non-metallic composite housing materials like G-10 fiberglass or carbon fiber could eliminate or substantially reduce eddy currents in the motor housing with limited mass impact. For the concept design here, the housing is aluminum and put at a radius of 0.5 m. The eddy currents losses in the housing are estimated to be on the order of a couple hundred Watts, but time-stepping 3D analysis would be required to obtain an accurate prediction.

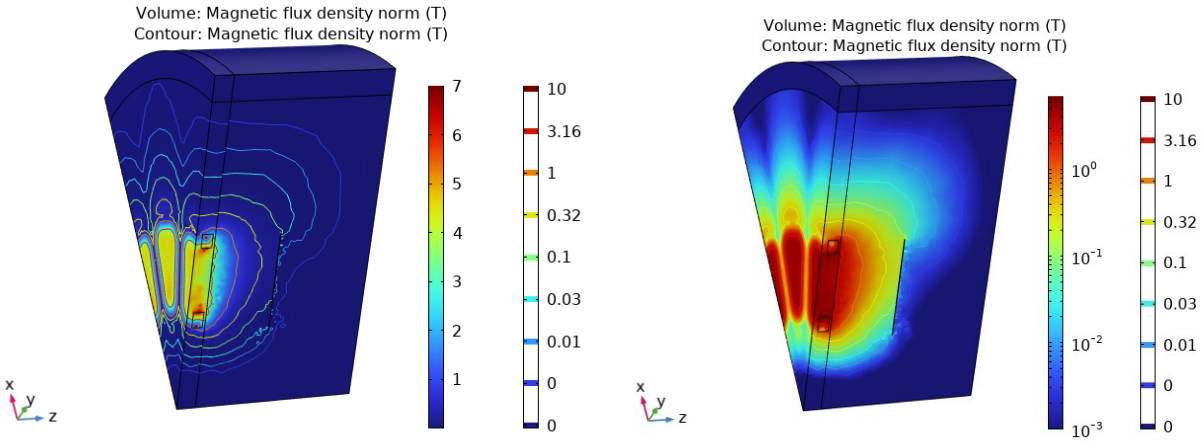

Fig. 19 3D magnetic FEA solution magnetic flux density plots showing the leakage radially out of the stator.

B. Higher-Fidelity Mechanical Analysis

Preliminary CAD of the machine is shown in Fig. 20. CAD is completed to a conceptual design level sufficient for using the geometries for mechanical FEA of the components and refining mass predictions. Details like fasteners and snap rings are neglected.

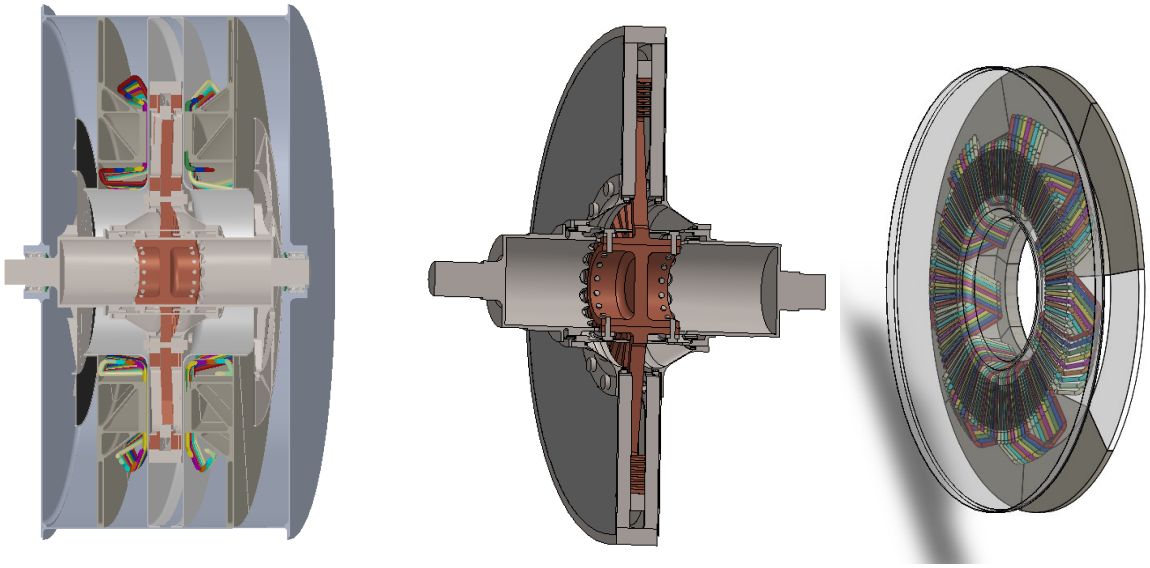

Fig. 20 Preliminary CAD of the axial machine. Left shows a cross sectional view of the full machine.

The mass of the machine in this preliminary CAD is estimated as 264 kg, roughly 30 kg heavier than that predicted by the refined design tool. This discrepancy has two primary sources. The first is that the radial 3D magnetic leakage was not accounted for in the design tool on this iteration. That leakage necessitates a bigger radius for the housing and requires the mating stator components to also expand radially. This factor accounts for roughly 18 kg of the mass discrepancy. The use of a non-metallic outer housing as discussed previously would allow the housing to be tighter to the machine and eliminate this mass error. Accounting for the radial leakage from this machine is a needed improvement to the design tool.

The second source of mass discrepancy is the addition of large containment hoops to react the centripetal and magnetic loading on the coils and to maintain pressure between the thermal bridges and the cold head, which was quantified with preliminary mechanical FEA. The addition of centripetal loading calculations for these retaining hoops in the next iteration of the design tool will improve its accuracy.

C. Higher-Fidelity Thermal Analysis

1. Stator Thermal Analysis

Combined fluid flow and thermal axisymmetric FEA on one stator was completed to verify the machine would close thermally. Fig. 21 shows the geometry of this simulation. A simplified 2D representation of the stator windings is used. A curvilinear coordinate system is solved for and used in the winding domain to maintain high thermal conductivity (~195 W/m-K) along the winding path and low thermal conductivity (3.8 W/m-K) perpendicular to the path. Epoxy is used to fill in the space within the winding end turns and as a stand-in material for the winding support structure. A rough representation of the fluid flow path maintaining close to a 1 mm channel around the winding is used.

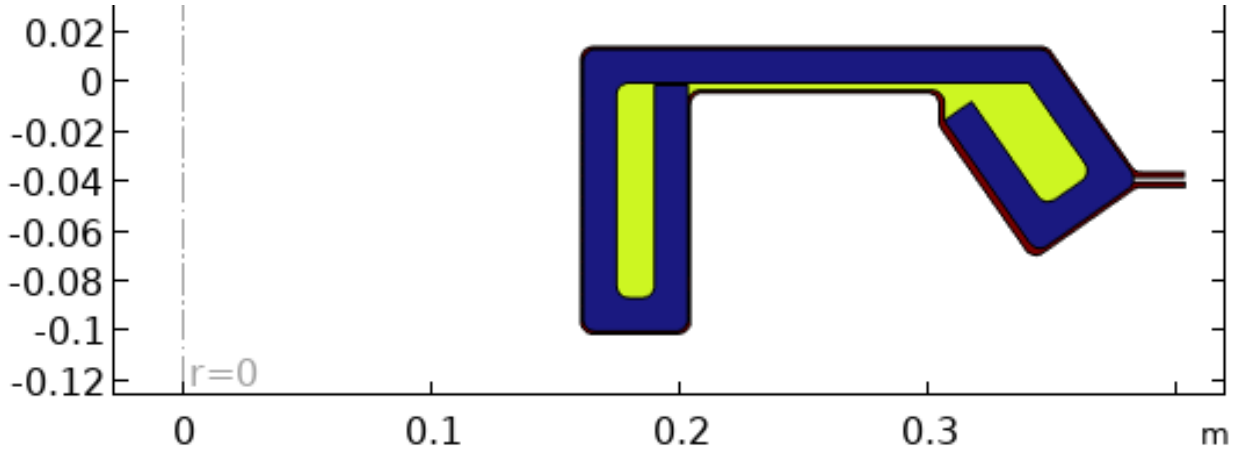

Fig. 21 Geometry for axisymmetric fluid flow and thermal simulation of the machine stator. Blue is the stator winding, yellow is epoxy filler/plastic support material, red is the fluid flow path.

Fig. 22 shows the fluid flow and thermal performance results for the machine. Significantly lower winding temperatures than estimated by the design code are predicted. The FEA model predicts a peak temperature of 116 °C whereas the design tool predicted 174 °C. There are two primary sources for the underprediction of the machine thermal performance by the design tool. The first is the low fidelity laminar prediction of the fluids cooling performance in the design tool. The second is that the design tool neglected the bend of the end windings in the areas it used for the thermal reluctance model and correspondingly underestimated the available cooling surface area. The model's boundary conditions, and geometry used here were idealized, and more detailed design could shift the results.

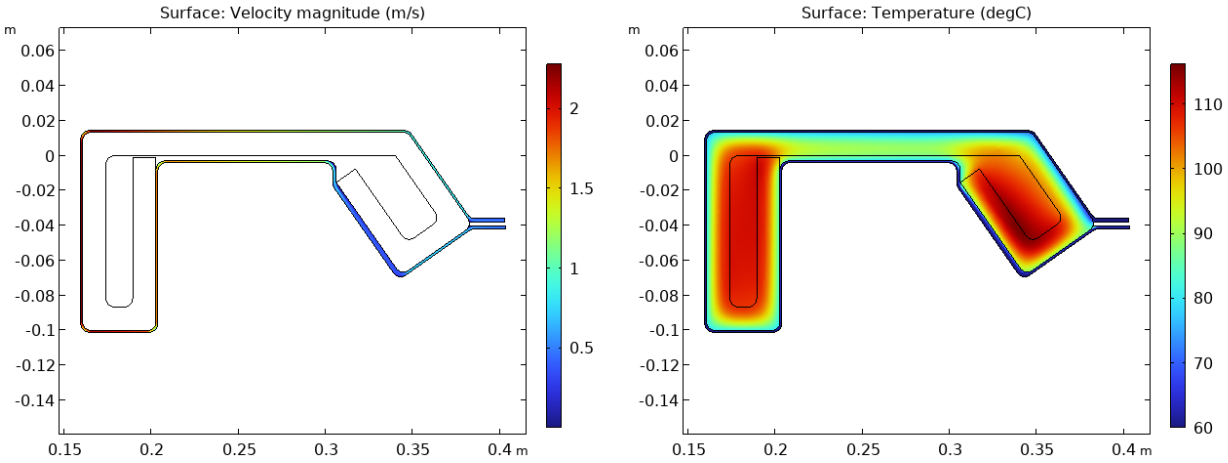

Fig. 22 Axisymmetric fluid flow and thermal simulation FEA results. Left shows fluid velocity. Right shows the temperature distribution.

Fig. 23 shows the results of a parametric sweep of the thermal model where stator current is increased. Here, the machine's power and efficiency are quantified assuming power increases proportionally with stator torque. The machine is shown to still be able to close thermally (stator winding temperature below 190 °C) to around a power of 7 MW. The machine is not able to maintain 99% efficiency at these higher powers but the increase in loss is small (~12%).

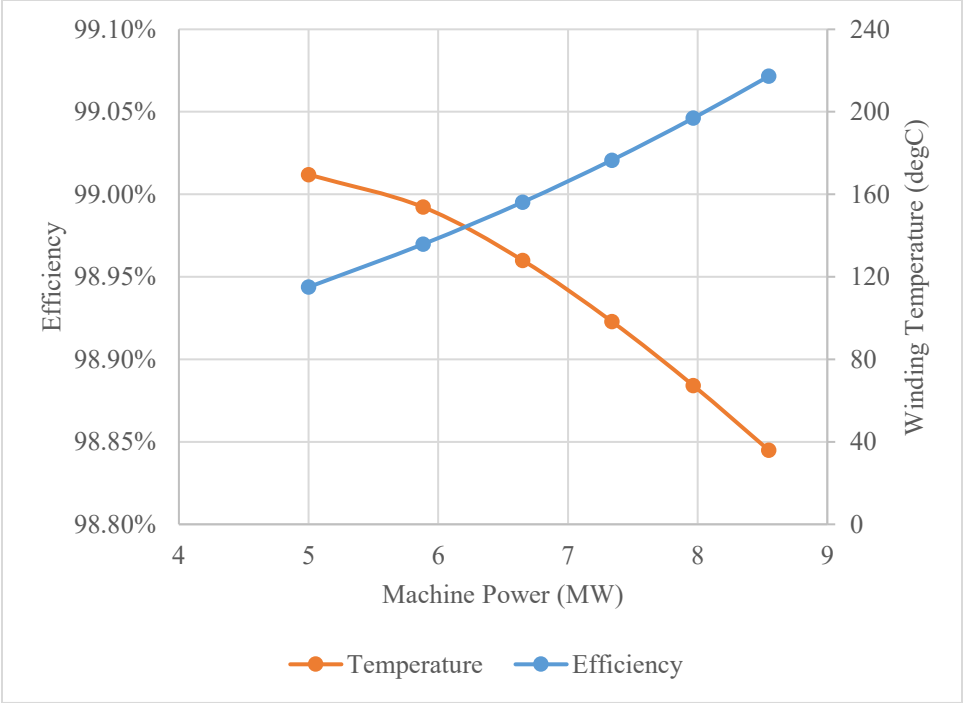

Fig. 23 Thermal model parametric sweep results for increases in stator current showing that the machine can close to around 7 MW.

2. Rotor Thermal Analysis

A preliminary 3D FEA thermal model of the rotor was completed to assess the accuracy of the design tool's thermal predictions. Fig. 24 shows the model's geometry and results. A sector of the rotor and shaft corresponding to half of one rotor pole is modeled. Axial symmetry of the machine is taken advantage of to further reduce model size. Temperature boundary conditions of 26.73 K to the cold head and 333 K to the inner diameter of the shaft are applied. Radiation boundary conditions with an assumed external temperature of 343 K are applied to all outward exposed surfaces of the rotor and shafts. Heat loads corresponding to the current leads (15 W), estimated resistive loss in coil-to-coil connections (1 W), and the estimated eddy current heat load (15 W) are applied to the model in the cold head, thermal bridge, and face plate of the rotor, respectively. Approximate thermal contact conductances are used at all interfaces. The approximate thermal conductances could be a key source of error in the model.

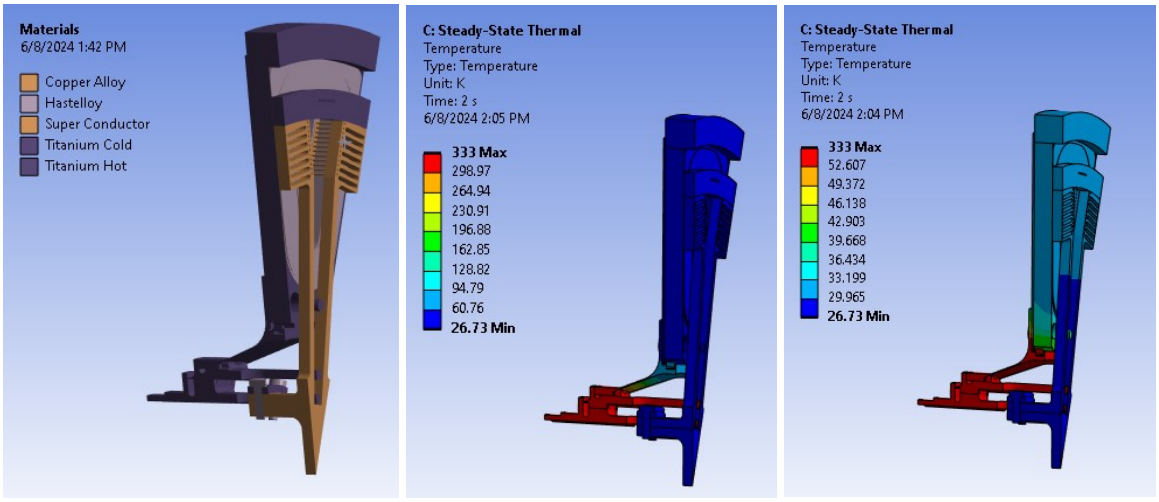

Fig. 24 Preliminary rotor thermal model result. Left shows the model geometry. Middle shows the full temperature distribution on a linear scale. Right shows the cold temperature distribution with everything above 52.6 K colored red.

Fig. 25 shows that the model predicts a temperature distribution in the rotor coil of about 31 to 33.5 K. This temperature is well below that of the design tool (37.6 K), thereby providing additional margin in the superconductor. The estimated heat load for the full machine into the cold head from the model is 65.4 W, which is equal to the expected heat load (Table 2) and below the lift of the cryocooler at the design temperature but has less margin than desired given the fidelity of the model. If this design was going to be prototyped, further model refinement would be needed to increase confidence in the rotor's thermal performance. In particular, mechanical refinement of the thermal bridge design would be needed to ensure adequate mechanical contact to the cold head. The model is sufficient to show that the design tool's thermal predictions for the rotor are reasonable. An area of improvement for the design tool is to add in approximate heat leak calculations based on the rotor's geometry rather than using a fixed estimate (25 W here).

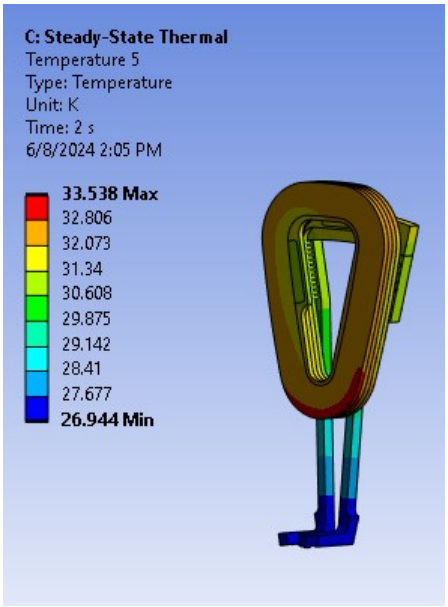

Fig. 25 Preliminary thermal model result showing the temperature distribution in the coils and thermal bridge.

VII. Conclusion

In this paper, an axial-flux partially-superconducting machine concept design iteration was documented. Details of a preliminary design tool for the machine topology were discussed and the tool, along with tools for radial machine counterparts, was exercised for a target electric aircraft application. A conceptual design was selected and detailed with higher-fidelity models of the machine. The concept design had a predicted performance of 19 kW/kg and 99% efficiency vs the expected 21 kW/kg and 99% efficiency from the design tool. Key areas for future refinement to improve the design tool accuracy include:

- Accounting for the radial 3D flux leakage in the machine either by adding the necessary additional radius to the machine housing, switching to non-metallic housing structures, or adding some form of shielding.
- Increasing the fidelity of the rotor mechanical structure in the design tool to better account for the centripetal loading on the coils and thermal bridge components.
- Increasing the fidelity of the thermal model. The low-fidelity approach used in this iteration appears to be overly conservative. Higher fidelity modeling showed that the concept machine could output steady state powers of approximately 7 MW and corresponding specific powers of ~25 kw/kg, but at the cost of ~0.1% efficiency. Including a better thermal model may allow the optimization to close closer to 25 kW/kg and 99% efficiency at 5 MW.

The results of this study will be incorporated into the next iteration conceptual design.

Appendix

A. Machine Topologies

Fig. 26-Fig. 30 depict the various machine topologies studied in this paper.

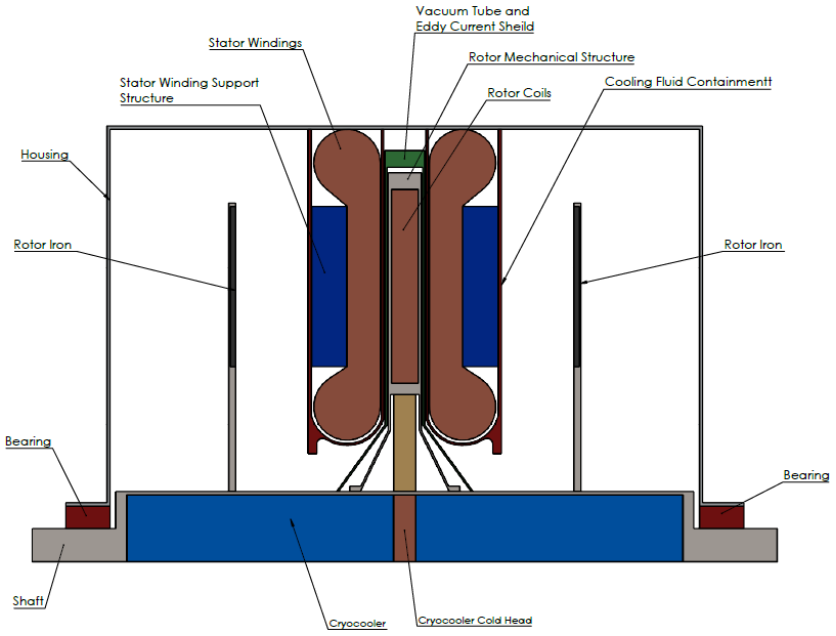

Fig. 26 Topology of the baseline axial-flux machine.

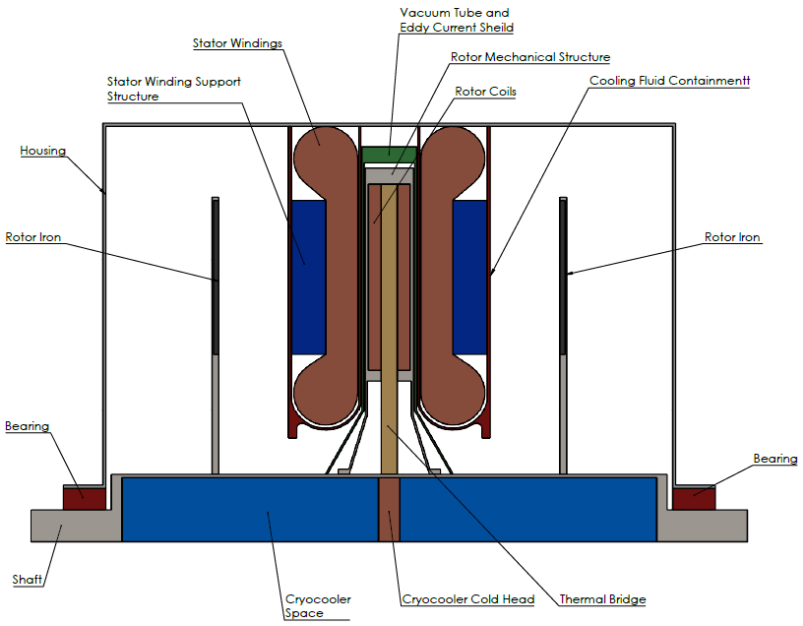

Fig. 27 Topology of the single-stack, mid-bridge, axial-flux machine.

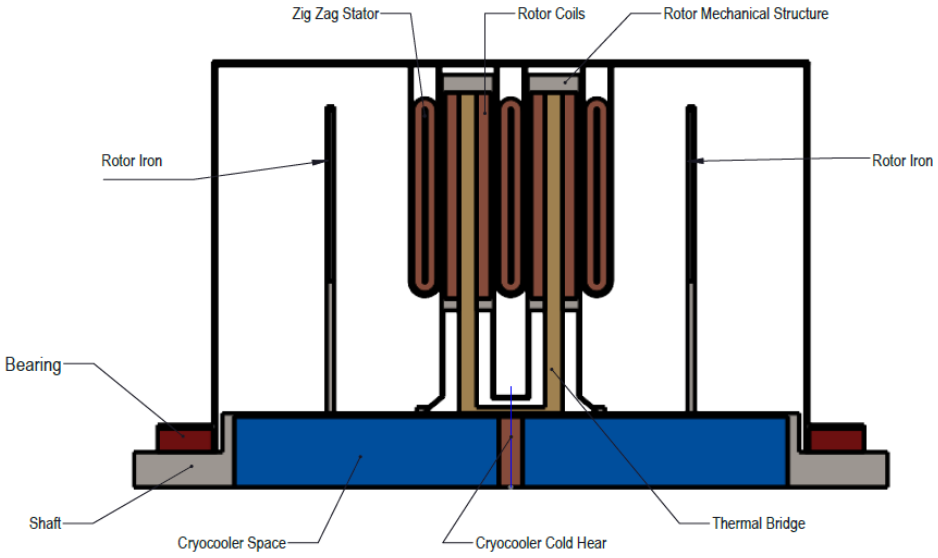

Fig. 28 Topology of the multi-stack, mid-bridge, axial-flux machine.

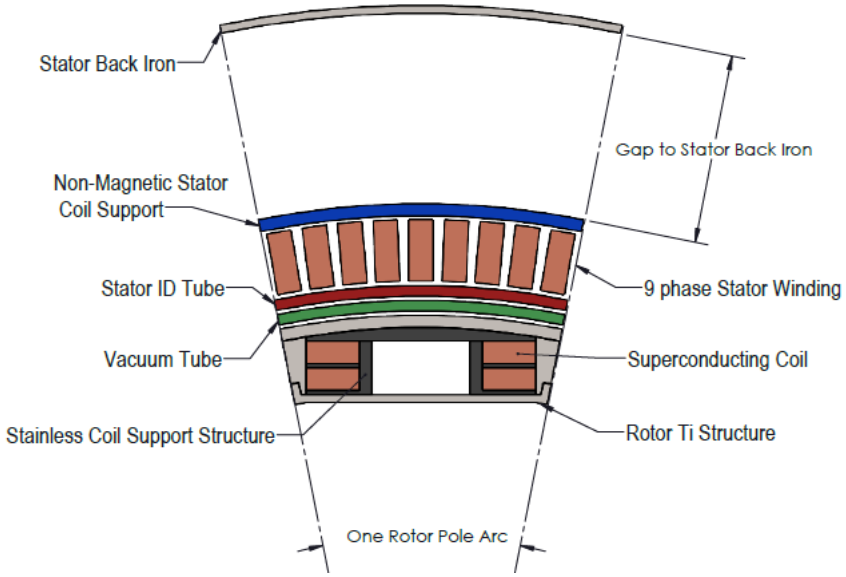

Fig. 29 Topology of the radial-flux, air-core machine.

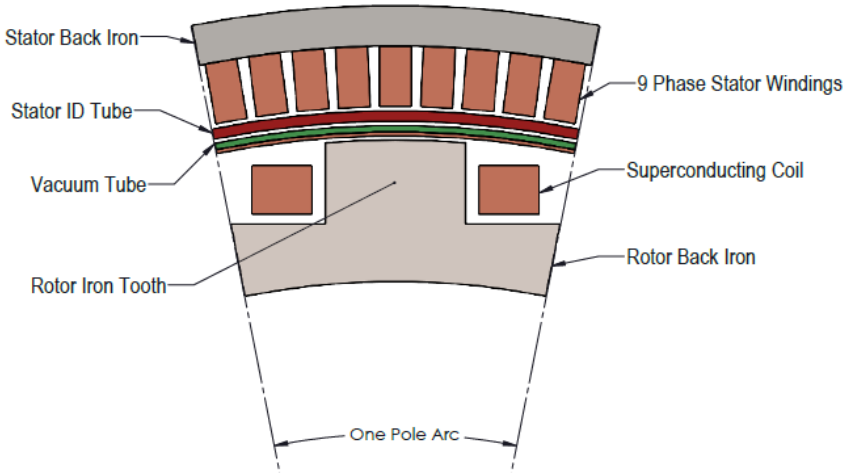

Fig. 30 Topology of the radial-flux, iron-core machine.

B. Current Lead Wire Optimization

To obtain estimates of the heat load passed to the cryocooler through the rotor's current lead wires, an optimization was carried out to design lead wires for various relevant rotor currents. A genetic algorithm was used to optimize the wires to minimize the heat load on the cryocooler. Only two parameters were used to define the lead, the length and the radius of the wire. A one-dimensional thermal reluctance network was used to represent the current lead wires for the optimization. Ten reluctance elements and 11 nodes were used. The cold node at the cryocooler cold head was assumed to be at 26 K and the hot end of the current lead was assumed to be at 353 K. The model was solved iteratively with the thermal conductivity of the lead and the resistive heat generated at each node estimated based on the temperature of the node from the previous iteration. Assuming a copper material for the lead wire, the electrical resistivity of the lead at each node was estimated as

$$\rho_{copper} = 1.72 * 10^{-8} * (1 + 4 * 10^{-3}(T - 293))$$

where ρ_{copper} is copper's electrical resistivity and T is the node temperature in units of K. The thermal conductivity of the nodes was estimated as

$$k_{copper} = 183837 * T^{-1.176}$$

where k_{copper} is the thermal conductivity of the lead at a given node in units of W/m-K.

The model is run for 5 iterations to converge. Heat load into the cold side of the model was extracted after the 5 iterations, doubled to account for both positive and negative current leads, and then used to define the fitness of a

given set of genetic input parameters. A minimum lead length of 75 mm was assumed. Optimizations were carried out for currents of 50 to 400 A in increments of 50 A. Table 3 provides the optimum design info for each iteration. Fig. 31 shows the heat performance of each design considered by the optimizer. Fig. 32 shows the curve fit of cryocooler heat load and mass from the optimization results.

Table 3 Lead wire optimization results.

I (A)	Radius (m)	Length (m)	Mass (kg)	Heat to Cryocooler (W)
50	0.0005	0.0842	0.0006	5.33
100	0.0005	0.0408	0.0003	10.66
150	0.0005	0.0272	0.0002	15.99
200	0.0005	0.0220	0.0002	21.32
250	0.0007	0.0315	0.0004	26.65
300	0.0005	0.0148	0.0001	31.97
350	0.0006	0.0161	0.0002	37.30
400	0.0008	0.0269	0.0005	42.63

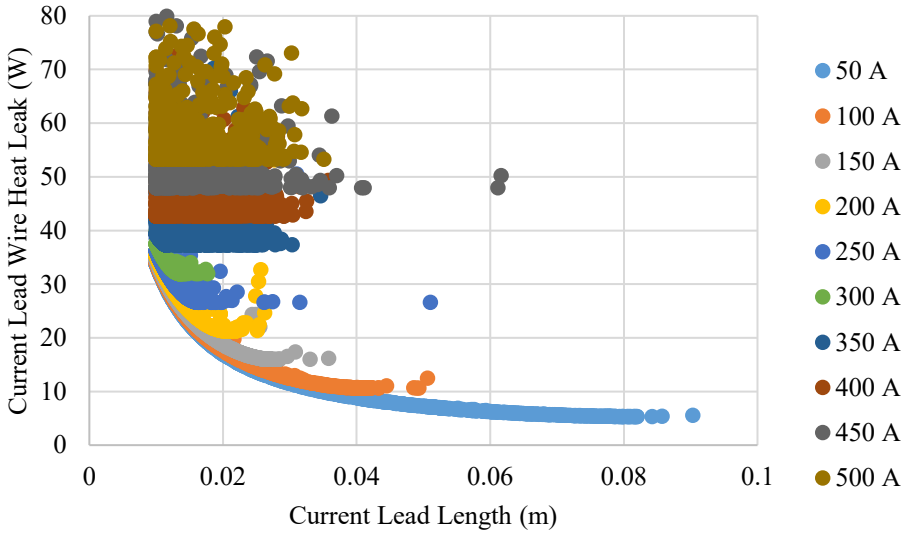

Fig. 31 Current lead heat versus lead length optimization results at different rotor currents.

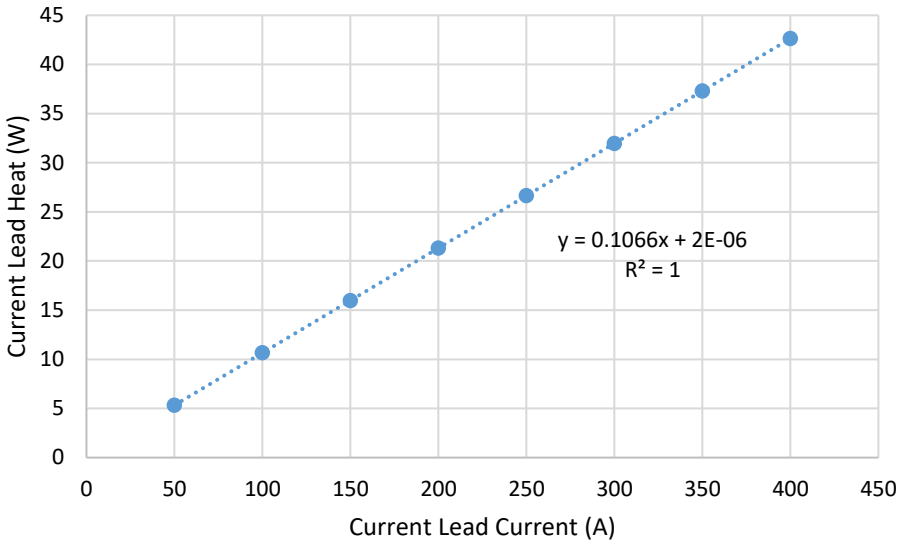

Fig. 32 Current lead wire heat leak versus rotor current.

Acknowledgments

The authors acknowledge NASA's Advanced Air Transportation Technology Project for funding this work.

VIII.References

[1] K. P. Duffy and R. Jansen, "Partially Turboelectric and Hybrid Electric Aircraft Drive Key Performance Parameters," in *AIAA/IEEE Electric Aircaft Technologies Symposium*, Cincinnati, 2019 .

[2] R. H. Jansen and et. all, "Subsonic Single Aft Engine (SUSAN) Transport Aircraft Concept and Trade Space Exploration," in *AIAA SciTech Forum*, San Diego, 2022.

[3] J. M. Haglage, T. P. Dever, R. H. Jansen and M. A. Lewis, "Electrical System Trade Study for SUSAN Electrofan Concept Vehicle," in *AIAA SciTech Forum*, Sna Diego, 2022.

[4] J. W. Chapman, J. L. Kratz, T. P. Dever, A. Mirhashemi, E. J. Stalcup, W. R. Sixel, A. A. Woodworth, R. H. Jansen and N. Heersema, "Update on SUSAN Concept Vehicle Power and Propulsion System," in *AIAA SCITECH 2023 Forum*, National Harbor MD, 2023.

[5] T. F. Tallerico, A. D. Anderson, J. J. Sheidler, R. Jansen and W. Sixel, "Concept Design of a 5 MW Partially Superconducting Generator," in *AIAA Aviation Forum*, San Diego CA, 2023.

[6] J. Scheidler and T. Tallerico, "Methodology for Electromagnetic Optimization of a Partially Superconducting 1.4 MW Electric Machine for Electrified Aircraft Propulsion," *IEEE Transactions on Applied Superconductivity,* vol. 33, no. 5, pp. 1-5, 2023.

[7] T. Tallerico, A. Anderson and J. J. Scheidler, "Design Optimization Studies of Partially Superconducting Machines based on NASA's High Efficiency Megawatt Motor," in *AIAA Propulsion and Energy Forum*, Virtual, 2021.

[8] R. H. Jansen, Y. De Jesus-Arce, P. Kascak, R. Dyson, A. Woodworth, J. J. Sheidler, R. Edwards, E. Stalcup, J. Whilhite, K. Duffy, P. Passe and S. McCormick, "High Efficiency Megawatt Motor Conceptual Design," in *AIAA Propulsion and Energy Forum*, Cincinnati, 2018.

[9] R. H. Jansen, P. Kascak, R. Dyson, A. Woodworth, J. Scheidler, A. D. Smith, T. Tallerico, Y. De Jesus-Arce, D. Avanesian, K. Duffy, P. Passe and G. Szpak, "High Efficiency Megawatt Motor Preliminary Design," in *AIAA/IEEE Electric Aircraft Technologies Synmposium*, Indianapolis, 2019.

[10] T. Tallerico, J. J. Scheidler, D. Lee and K. S. Haran, "Electromagnetic Redesign of NASA's High Efficiency Megawatt Motor," in *AIAA/IEEE Electric Aircraft Technologies Symposium*, Virtual, 2020.

[11] G. Szpak, A. Smith, J. T. Thompson, A. Woodworth and R. Jansen, "High Efficiency Megawatt Motor Thermal Stator Preliminary Design," in *AIAA/IEEE Electrified Aircraft Technologies Symposium*, New Orleans, 2020.

[12] J. J. Scheidler, "Preliminary Design of the Superconducting Rotor for NASA's High-Efficiency Megawatt Motor," in *AIAA Propulsion and Energy Forum*, Cincinnati, 2018.

[13] R. W. Dyson, R. H. Jansen, K. P. Duffy and P. J. Passe, "High Efficiency Megawatt Machine Rotating Cryocooler Conceptual Design," in *AIAA Propulsion and Energy Forum*, Indianapolis, 2019.

[14] R. H. Jansen, J. Scheidler, T. Tallerico, P. Kascak, A. Woodworth, A. Smith, R. Dyson, W. Sixel, J. Thompson, E. Stalcup, Y. De Jesus-Acre, D. Avanesian, K. Duffy, P. Passe and G. Szpak, "High Efficiency Megawatt Motor Risk Reduction Activities," in *Electrified Aircraft Technologies Symposium*, New Orleans, 2020.

[15] T. Tallerico, A. Anderson, M. Hurrell and M. Valco, "Preliminary Measurements of Partial Discharge Inception Voltage Degradation with Constant Temperature Aging of Magnet Wire Twisted Pairs for Electric Aircraft Motors," NASA, Cleveland, 2023.

[16] M. G. Granger, A. Aaron, J. M. Maroli, T. Tallerico and J. J. Scheidler, "Combined Analysis of NASA's High Efficiency Megawatt Motor and Its Converter," in *AIAA Propulsion and Energy Forum*, Virtual, 2021.

[17] M. Granger and a. et, "Concept Design of a 1.4 MW Drive for Rotor Loss Minimization in a Partially Superconducting Motor," in *IEEE Transportation Electrification Conference & Expo (ITEC)*, Anaheim, 2022.

[18] E. Stalcup, J. Scheidler, T. Tallerico, W. Torres, K. Dufy and T. Mulder, "Thermal Design, Analysis, and Testing of a Conductively-Cooled, High Temperature Superconducting Rotor for a 1.4 MW Electric Machine for Aeronautics Applications," in *Thermal and Fluids Analysis Workshop (TFAWS)*, College Park, MD, 2023.

[19] J. Scheidler, E. Stalcup, T. Tallerico, W. Torres, K. Duffy and T. Mulder, "Cryogenic Vacuum Chamber Testing of A Conductively-Cooled, High Temperature Superconducting Rotor for a 1.4 MW Electric Machine for Aeronautics Applications," in *25th Joint Cryogenic Engineering Conference and International Cryogenic Materials Conference (CEC/ICMC)*, Honolulu, HI, 2023.

[20] J. Scheidler, E. Stalcup, T. Tallerico, T. Mulder, W. Torres and K. Duffy, "Static testing of a conductively-cooled, high temperature superconducting rotor for a 1.4 MW electric machine in a thermal vacuum chamber," in *AIAA Aviation 2023 Forum*, Sand Diego, CA, 2023.